Journal of Materials Chemistry A

Bi Catalysts Supported on GaN Nanowires toward Efficient Photoelectrochemical CO2 Reduction

Journal:	*Journal of Materials Chemistry A*
Manuscript ID	TA-ART-01-2022-000032.R2
Article Type:	Paper
Date Submitted by the Author:	14-Feb-2022
Complete List of Authors:	Dong, Wan Jae; University of Michigan, ; POSTECH, Navid, Ishtiaque; University of Michigan, Department of Electrical Engineering and Computer Science Xiao, Yixin; University of Michigan, Department of Electrical Engineering and Computer Science Lee, Tae Hyung; Seoul National University, Department of Materials Science & Engineering Lim, Jin Wook; POSTECH, Material Science & Engineering Lee, Donghwa; Pohang University of Science and Technology, Materials Science and Engineering Jang, Ho Won; Seoul National University, Department of Materials Science and Engineering, Research Institute of Advanced Materials Lee, Jong-Lam; POSTECH, Material science and engineering Mi, Zetian; University of Michigan

SCHOLARONE™
Manuscripts

PAPER

Bi Catalysts Supported on GaN Nanowires toward Efficient Photoelectrochemical CO_2 Reduction

Received 00th January 20xx,
Accepted 00th January 20xx

DOI: 10.1039/x0xx00000x

Wan Jae Dong,[a,b,‡] Ishtiaque Ahmed Navid,[a,‡] Yixin Xiao,[a] Tae Hyung Lee,[c] Jin Wook Lim,[b] Donghwa Lee,[d] Ho Won Jang,[c,*] Jong-Lam Lee,[b,*] Zetian Mi[a,*]

Photoelectrodes combined with semiconductors and cocatalysts have been extensively investigated for photoelectrochemical reduction of CO_2 gas to chemicals and fuels. However, little attention has been paid to the electronic interaction between semiconductor photoelectrode and cocatalyst, which is critical for controlling the CO_2 reduction reaction. Here, we have discovered that the unique electronic interaction at the interface between bismuth nanoparticles (Bi NPs) and gallium nitride nanowires (GaN NWs) can significantly boost the catalytic activity for CO_2 reduction reaction on a silicon photocathode. Theoretical calculations suggest that the binary system consisting of Bi and GaN favors CO_2 conversion to HCOOH and enhances electron transfer from GaN NWs to Bi NPs. The optimized Bi/GaN/Si photocathode results in a superior faradaic efficiency of HCOOH (FE_{HCOOH}) ~98% at -0.3 V_{RHE} under 1-sun light illumination.

Introduction

The ever-increasing CO_2 emissions associated with fossil-based energy consumption have led to serious environmental concerns. CO_2 reduction reaction (CO_2 RR) has been considered as a promising solution to overcome this challenge.[1] To improve the activity of CO_2 RR, many electrocatalysts have been developed and achieved relatively high selectivity and productivity at low overpotential for single-carbon (CO, CH_4, and HCOOH)[2, 3, 4, 5] and multi-carbon products (C_2H_4, C_2H_6, and C_2H_5OH).[6, 7, 8] When the electrocatalysts were integrated with renewable energy sources, net CO_2 reduction could be potentially realized while simultaneously producing value-added feedstock. Therefore, solar-driven photoelectrochemical (PEC) CO_2 RR based on semiconductor photoelectrode is believed to be one of the most attractive approaches because of solar energy's infinite reservoir and environmental benignancy. Previously, various kinds of semiconductors such as Si,[9, 10, 11] III-V,[12] and metal oxides[13, 14, 15] have demonstrated PEC CO_2 RR. However, these semiconductors usually suffer from insufficient light absorption, sluggish charge carrier transport, photocorrosion, or most importantly poor catalytic activity.[16, 17] Therefore, surface cocatalyst has been required to improve the catalytic activity of PEC CO_2 RR.

Noble metals such as Au,[18, 19] Ag,[20, 21] and their alloys[22, 23] have been frequently decorated on photocathodes as cocatalysts. However, these noble metals are too expensive for practical application. To replace the noble metals, inexpensive and earth-abundant cocatalysts have been studied and developed for electrocatalytic CO_2 RR. Especially, Sn and Bi metals have shown promise for converting CO_2 to formic acid (HCOOH).[10, 24, 25, 26] However, the effective utilization of earth-abundant cocatalysts in PEC CO_2 RR still remains a grand challenge due to the inefficient light trapping, limited surface area, poor stability, and insufficient activity of semiconductor photocathodes.[18, 24, 25] Recently, single-crystal GaN nanowires (GaN NWs) vertically grown on Si photocathodes have emerged as an efficient and stable platform to achieve high performance CO_2 RR as well as water splitting. [27, 28, 29, 30, 31] To date, however, there have been few studies of interfacial interactions between semiconductor and cocatalyst to further improve the performance.

For heterogeneous catalysis, tuning the electronic structure has been an important strategy to improve the catalytic activity.[32, 33, 34, 35, 36, 37, 38, 39] Interfacial interaction between two different materials changes the electronic structure, alters the binding energies of reaction intermediates, and consequently tunes the catalytic pathway. Therefore, a fine control over the composition and structure of multi-composite catalysts can yield unique catalytic properties that cannot be obtained with a single catalyst material.[34, 40, 41, 42] However, little attention has been paid to the interfacial electronic effects induced by interaction between semiconductor and cocatalyst on PEC catalysis, owing to the complexity of heterogeneous interface, difficulty of fabricating high-quality semiconductor material, and poor stability of conventional photocathodes in aqueous media. Thus, a fundamental understanding of the electronic modulation by interfacial interaction is critical and urgently needed in order to control the selectivity, productivity, and stability of PEC CO_2 RR.

---

[a] Department of Electrical Engineering and Computer Science, University of Michigan, 1301 Beal Avenue, Ann Arbor, MI 48109, USA
[b] Department of Materials Science and Engineering, Pohang University of Science and Technology (POSTECH), Pohang 37673, Korea
[c] Department of Materials Science and Engineering, Research Institute of Advanced Materials, Seoul National University, Seoul 08826, Korea
[d] Division of Advanced Materials Science, Pohang University of Science and Technology (POSTECH), Pohang 37673, Korea

‡These authors contributed equally to this work.

Electronic Supplementary Information (ESI) available: [details of any supplementary information available should be included here]. See DOI: 10.1039/x0xx00000x

Here, we have investigated the electronic interaction between Bi NPs and GaN NWs grown on planar Si wafer and the impact on PEC CO_2 RR. The unique atomic ordering and electronic properties of defect-free GaN NWs showed enormous promise for efficient CO_2 conversion when integrated with Bi NPs cocatalysts. X-ray photoelectron spectroscopy (XPS) measurement and density functional theory (DFT) calculation suggested strong electronic interaction by sharing the electrons between Bi NPs and GaN NWs. This interaction lowered the thermodynamic reaction barriers and further facilitated electron transport. The reaction mechanism of the Bi/GaN system is different from the previous CO_2 RR over Bi electrocatalysts or GaN photocathodes. As a result, the integration of Bi NPs on GaN NWs greatly improved faradaic efficiency of HCOOH (FE_{HCOOH}) ~98% at -0.3 V_{RHE}, achieved a high current density of HCOOH (j_{HCOOH}) = 10.3 mA/cm^2 at -0.6 V_{RHE}, and operated 12 h without degradation under 1-sun light illumination.

Results and discussion

Bi/GaN/Si photocathodes were fabricated by plasma-assisted molecular-beam epitaxy (MBE) growth of single-crystal GaN NWs on n^+-p silicon substrate, followed by thermal evaporation of Bi NPs (Fig. 1a). Scanning electron microscopy (SEM) images showed the vertically grown GaN NWs on the planar n^+-p Si wafer (Fig. S1). The average length of GaN NWs was ~288 nm and the average diameter was ~60 nm (Fig. 1b and Fig. S2). After the decoration of 10 nm-thick Bi NPs, the surface morphology of GaN NWs was roughened (Fig. 1c). The presence of Bi NPs was further confirmed by energy-dispersive X-ray spectroscopy (EDS) analysis (Fig. S3). X-ray diffraction (XRD) patterns of GaN/Si and Bi/GaN/Si showed GaN (002), GaN (004), and Si (004) peaks (Fig. S4).[43] Because the grains size of Bi NPs was too small, the XRD peaks from Bi NPs cannot be detected.

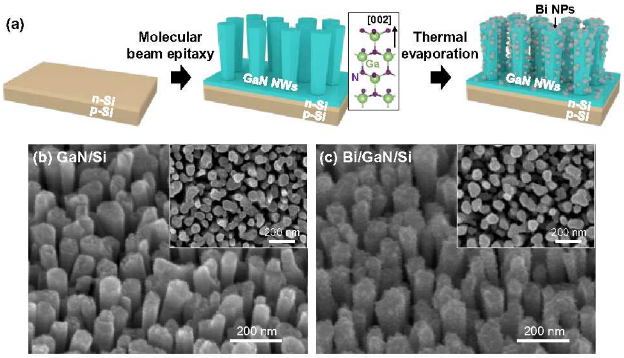

Fig. 1 (a) Schematic illustration of the fabrication of Bi/GaN/Si photocathode by MBE growth of single-crystal GaN NWs on Si p-n wafer and thermal evaporation of Bi NPs. 45°-tilted-view and top-view (inset) SEM images of (b) GaN/Si and (c) Bi/GaN/Si.

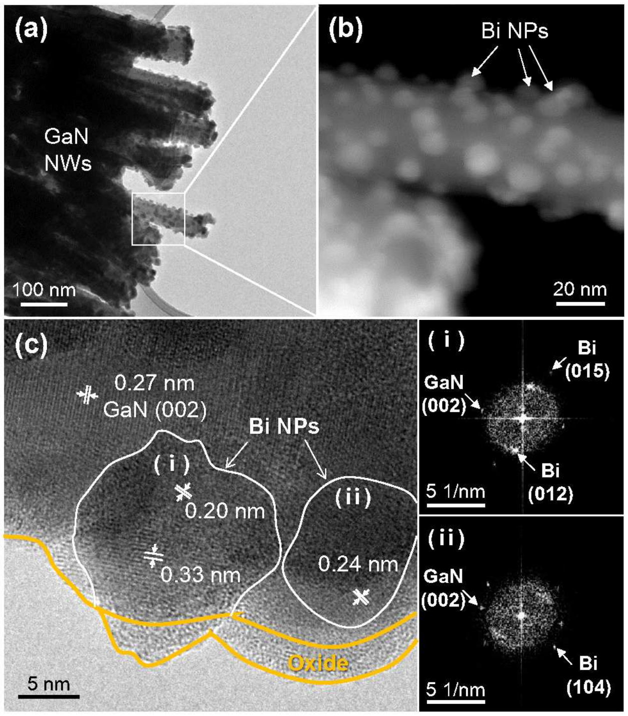

Fig. 2 (a) TEM and (b) HAADF-STEM images of Bi/GaN/Si. (c) High-resolution TEM image and electron diffraction patterns at Bi/GaN interface. Polycrystalline Bi NPs were uniformly distributed on single-crystal GaN NWs and ~2 nm amorphous oxide was formed on the surface of Bi NPs.

In order to confirm the microstructure and atomic distribution of GaN NWs and Bi NPs, we performed scanning transmission electron microscopy (STEM) studies. Bi NPs uniformly distributed on the array of GaN NWs (Fig. 2a). Because the atomic number differences between Ga (31) and Bi (83) are fairly large, we could obtain sufficient Z-contrasts from the locally segregated Bi NPs on GaN NWs in the high angular annular dark field (HAADF)-STEM images (Fig. 2b). In the STEM images, the size of Bi NPs was statistically calculated by computer software and the average size was measured to be 9.1 nm (Fig. S5). High-resolution transmission electron microscope (HR-TEM) images and selected area electron diffraction patterns also evidenced the Bi NPs on GaN NWs (Fig. 2c and Fig. S6). Lattice fringes were observed with d-spacings of 0.20, 0.24, 0.27, and 0.33 nm, which correspond to Bi (015), Bi (104), GaN (002), and Bi (012) planes, respectively (JCPDS #02-1078 and #44-1246). This indicates that polycrystalline Bi NPs were formed on single-crystal GaN NWs. Moreover, the surface of Bi NPs was covered with ~2 nm-thick amorphous oxide, indicating a metal/oxide core/shell structure.

Morphology of Bi NPs was investigated after CO_2 RR for 20 min at -0.4 V_{RHE} in 0.1 M $KHCO_3$. The presence of Bi NPs having the size of 3-20 nm was evident on GaN NWs, indicating that Bi NPs were stably anchored on the surface of GaN NWs without a noticeable change in morphology (Fig. S7a,b). Crystallographic orientations of Bi NPs were investigated by lattice fringes and electron diffraction patterns. Bi (012) plane with a lattice spacing of 0.33 nm (Fig. S7c), $Bi_2O_2CO_3$ (013) plane with a lattice spacing of 0.30 nm (Fig. S7d), and Bi_2O_3 (002) plane with a lattice spacing of 0.35 nm (Fig. S7e) were observed. The outermost surface of cocatalysts was passivated by the amorphous region with thickness of 2-5 nm. The oxidized forms of $Bi_2O_2CO_3$, Bi_2O_3, and amorphous oxides might have been transformed from metallic Bi by immersing the sample in the aqueous electrolyte. There should be unavoidable partial reduction of the oxidized Bi species to metallic Bi during CO_2 RR. However, it is also true that bismuth-oxygen structure can remain during CO_2 RR at cathodic potentials as confirmed by operando Raman and in-situ X-ray absorption near-edge structure measurements.[26, 44, 45] Hence, we consider that Bi NPs acting in the catalytic reaction were composed of not only metallic Bi and but also oxidized forms.

X-ray photoelectron spectroscopy (XPS) was carried out to study the surface bonding states of photoelectrodes. Ga $2p_{3/2}$ XPS spectra were separated with a major peak of Ga-N bond (1118.0 eV) and a minor peak of Ga-O bond (1119.2 eV) (Fig. 3a).[46] After depositing Bi NPs, the peak intensity of Ga $2p_{3/2}$ XPS spectra reduced by ~4 times because Bi NPs screened the photoelectrons emitted from GaN NWs. Moreover, the Ga $2p_{3/2}$ spectrum of Bi/GaN/Si positively shifted ~0.21 eV compared to GaN/Si likely due to electron donation from GaN NWs to Bi NPs. After the CO_2 RR for 20 min in 0.1 M $KHCO_3$ at -0.4 V_{RHE}, XPS spectra were approximately the same. This suggests that the chemical bonding states of GaN NWs didn't change during the PEC CO_2 RR. In N 1s XPS spectra, N-Ga (398.4 eV) and N-O (399.8 V) bonds were detected with Ga LMM Auger electrons (Fig. 3b).[47] Similar to Ga $2p_{3/2}$ XPS results, the intensity of N 1s decreased after deposition of Bi NPs and shifted positively by ~0.31 eV, revealing electrons transfer and strong electronic interaction between GaN NWs and Bi NPs. Positive shift of Ga $2p_{3/2}$ and N 1s spectra implied that the GaN NWs donate electrons to Bi NPs. The spontaneous electron transfer from GaN NWs to Bi NPs will be discussed in detail in the following calculation section.

To elucidate the bonding states of Bi NPs, deconvolution of Bi 4f XPS spectra was carried out with metallic Bi^0 (156.4 and 161.7 eV) and Bi^{3+} (158.5 and 163.8 eV) bonds (Fig. 3c). GaN NWs showed a peak from Ga 3s electrons without the characteristic doublet peaks of Bi $4f_{7/2}$ and Bi $4f_{5/2}$ spectra. In contrast, Bi/GaN/Si exhibited a metallic Bi^0 peak and an intense Bi^{3+} peak. The Bi^{3+} peak retained on the surface even after the CO_2 RR due to spontaneously formed $Bi_2O_2CO_3$, Bi_2O_3, and amorphous oxides on the surface of Bi NPs in the aqueous electrolyte as described in TEM results. Despite there could be partial reduction of $Bi_2O_2CO_3$ and Bi_2O_3 during CO_2 RR, the Bi^{3+} states might dominate the outer surface layer where catalytic reaction occurs. To investigate the oxidation states of surface oxides, O 1s XPS spectra were fitted with four peaks of O-Ga (531.1 eV), O-Bi (529.4 eV), OH-Bi (530.9 eV), and absorbed H_2O (532.2 eV) (Fig. S8).[48] It was found that the oxide (O-Bi) and hydroxide (OH-Bi) were the reason for the Bi^{3+} peaks. Even after the PEC CO_2 RR, the presence of O-Bi and OH-Bi bonds showed that Bi oxides remain at the outmost layer of Bi NPs.

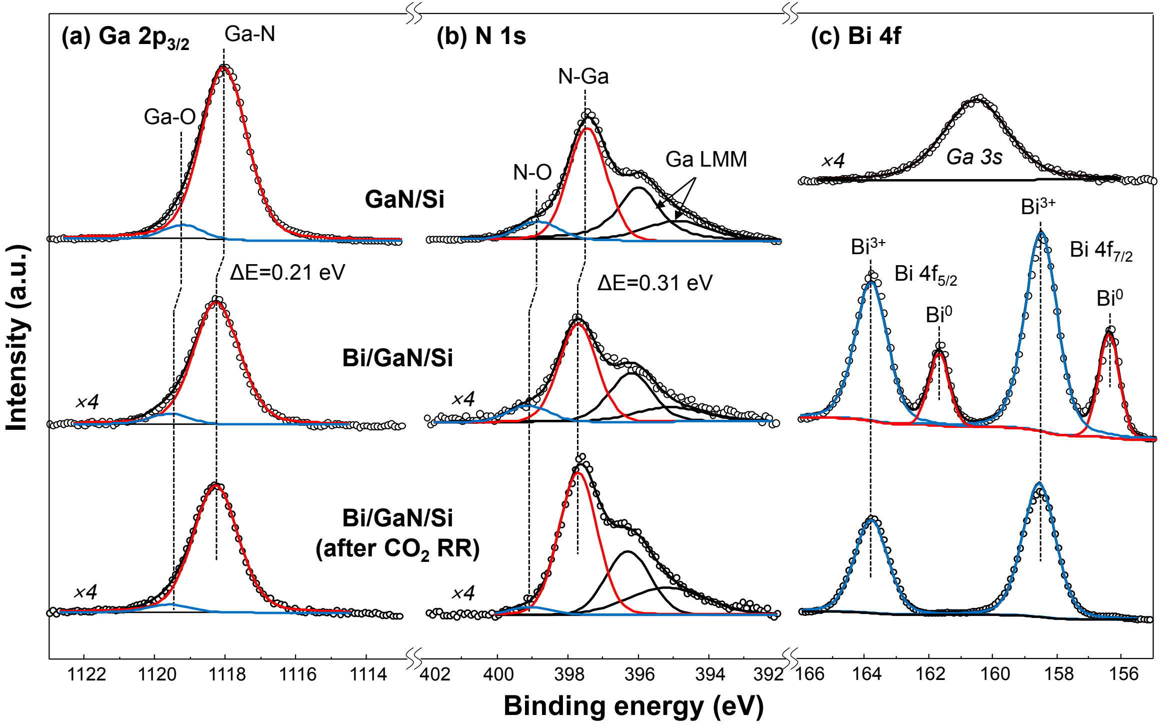

Fig. 3 XPS spectra of (a) Ga $2p_{3/2}$, (b) N 1s, and (c) Bi 4f for GaN/Si, Bi/GaN/Si, and Bi/GaN/Si photocathodes after CO_2 RR. The peak positions of Ga $2p_{3/2}$ and N 1s spectra positively shifted after coating of Bi NPs, indicating strong electronic interaction between GaN NWs and Bi NPs.

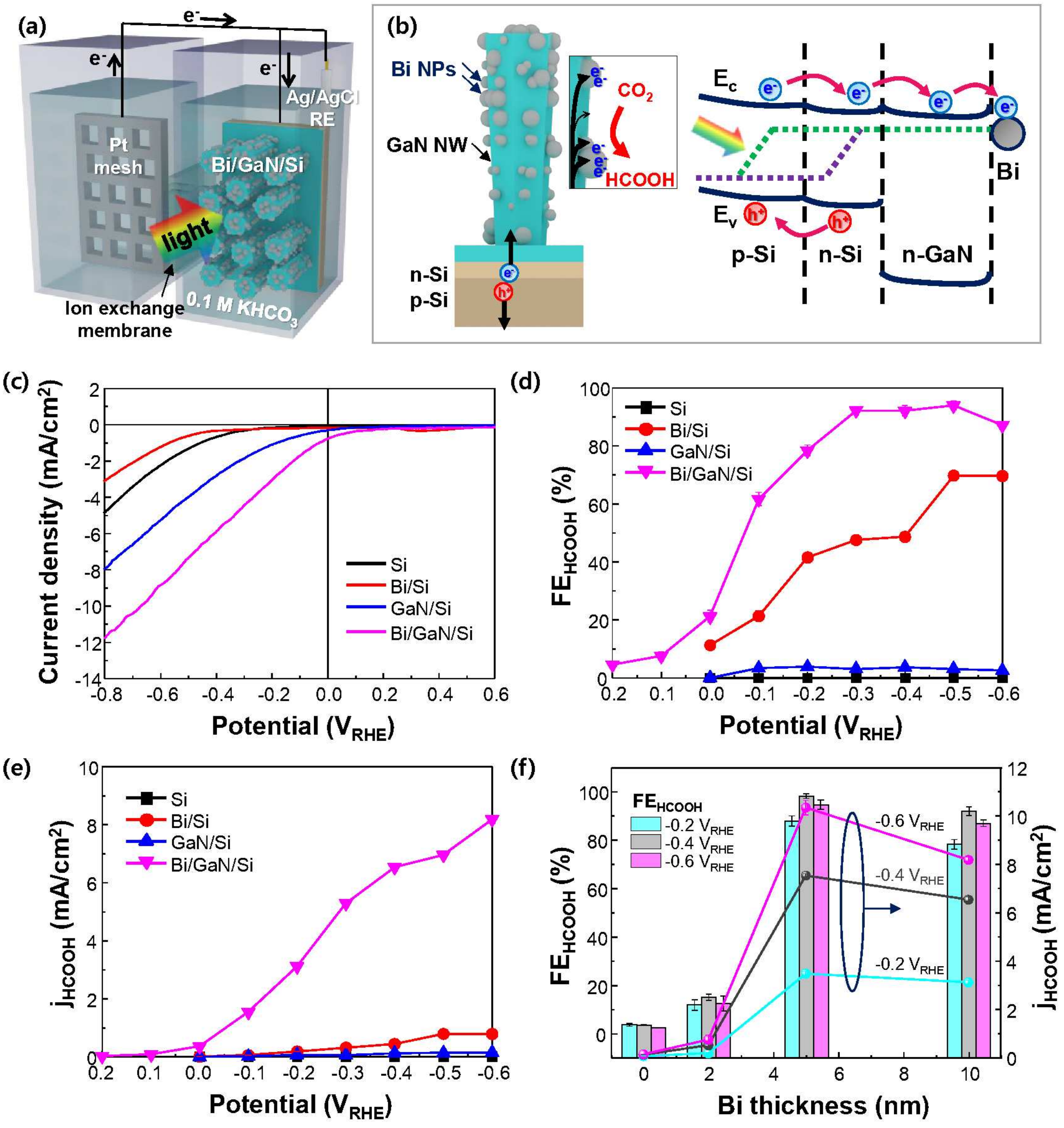

Fig. 4 Schematic illustrations of (a) PEC CO_2 RR and (b) energy band diagram of Bi/GaN/Si photocathode. (c) LSV curves, (d) FE_{HCOOH}, and (e) j_{HCOOH} of Si, Bi/Si, GaN/Si, and Bi/GaN/Si in CO_2-purged 0.1 M $KHCO_3$ electrolyte. The Bi thickness was 10 nm for Bi/Si and Bi/GaN/Si samples. (f) Bi thickness dependent FE_{HCOOH} (left axis) and j_{HCOOH} (right axis) of Bi/GaN/Si at potentials of -0.2, -0.4 and -0.6 V_{RHE}.

PEC CO_2 RR was performed by illuminating light (AM 1.5G 100 mW/cm²) on Bi/GaN/Si photocathode on the surface normal direction and applying electrical potential using a three-electrode configuration (Fig. 4a). The n^+-p Si wafer with a small bandgap (~ 1.1 eV) readily generates electron-hole pairs by solar irradiation. GaN NWs enhance the light trapping in the Si substrate by suppressing the reflection loss. The average optical reflectance (OR) of Si substrate was 51.4% at wavelengths of 400 ~ 800 nm (Fig. S9). In contrast, GaN NWs effectively reduced OR to 17.4% because their vertically-aligned structure matches the refractive indices between air and Si substrate.[49] In addition, Bi NPs with thickness (t_{Bi}) = 10 nm on GaN NWs functioned as a light scattering center, leading to enhanced light absorption and reduced OR to 11.7%. On the other hand, Bi film (t_{Bi} = 10 nm) formed on the planar Si wafer reflects the incident light and increased OR to 57.9% (Fig. S10). The vertically aligned NWs were found to be an excellent geometric framework to load the cocatalysts of Bi NPs and enhance the optical transmittance by preventing Fresnel reflection (Fig. S11). As shown in the energy band diagram of the photocathode, the transport of photoexcited electrons from Si to GaN is feasible without any significant barrier since conduction bands of n^+-Si and n^+-GaN are approximately aligned (Fig. 4b).[27] Therefore, photogenerated electrons can readily migrate toward active sites of Bi NPs to participate in CO_2 RR.

This journal is © The Royal Society of Chemistry 20xx

Linear sweep voltammetry (LSV) measurements were conducted to study the PEC CO_2 RR performance of planar Si, Bi/Si, GaN/Si, and Bi/GaN/Si in CO_2-purged 0.1 M $KHCO_3$ (Fig. 4c). The photocurrent densities (j) of Si and Bi/Si with t_{Bi} = 10 nm were smaller than those of GaN NWs due to the reflection loss and smaller surface area. Interestingly, GaN NWs grown on Si substrate showed a significant improvement in an onset potential (0 V_{RHE}) and j (~8.0 mA/cm^2 at -0.8 V_{RHE}) because of the efficient light trapping, effective charge carrier transport, and suppressed recombination. Furthermore, after deposition of Bi NPs on GaN NWs (t_{Bi} = 10 nm), j was further improved to 11.9 mA/cm^2 at -0.8 V_{RHE}. The photocathodes exhibited negligible activity in the dark condition, revealing that solar energy is required for the PEC reactions.

The influence of the applied potential on the FEs was investigated for Si, Bi/Si, GaN/Si, and Bi/GaN/Si (Fig. S12 and Table S1) and FE_{HCOOH} was summarized (Fig. 4d). Planar Si primarily produced H_2 with a little amount of CO (FE_{CO} < 10%). Deposition of Bi film on Si substrate (Bi/Si) generated HCOOH at 0 V_{RHE} and showed a maximum FE_{HCOOH} ~70% at -0.5 V_{RHE}. The GaN/Si photocathode predominantly produced H_2. However, Bi/GaN/Si greatly improved the selectivity of HCOOH and positively shifted the onset potential. High FE_{HCOOH} > 92% was achieved at -0.3 V_{RHE}, and the onset-potential was ~0.2 V_{RHE}. According to previous studies, the thermodynamic energy barrier for hydrogen evolution reaction (HER) on Bi catalyst was much higher than that of CO_2 reduction to HCOOH because the free energy of H adsorption was too positive to allow active HER.[50] Therefore, H adsorption on the Bi/GaN/Si photocathode was inhibited and HER should be largely suppressed. Since Bi/GaN/Si showed the best j and FE_{HCOOH} among the measured photoelectrodes, j_{HCOOH} was also the highest (Fig. S13). The maximum j_{HCOOH} of Bi/GaN/Si was 8.2 mA/cm^2 at -0.6 V_{RHE} which was ~10 times higher than that of Bi/Si (0.8 mA/cm^2) (Fig. 4e). What is more, Bi/GaN/Si showed the maximum applied bias photon-to-current efficiency (ABPE) of 0.15% at -0.1 V_{RHE} whereas the other photocathodes of Si, Bi/Si, and GaN/Si exhibited low ABPE < 0.01% (Fig. S14). In comparison to electrocatalytic performance of Bi film, Bi/GaN/Si photocathode showed enormously improved onset potential, current density, and FE_{HCOOH} under solar light (Fig. S15). Thus, the synergetic electronic interaction between GaN NWs and Bi NPs enhanced the conversion rate of CO_2 to HCOOH as well as the selectivity. Moreover, we measured the products in the anodic compartment to investigate the oxidation reactions at the counter electrode (Fig. S16). When we applied cathodic potential of -0.4 and -0.6 V_{RHE} to the photocathode for 20 min, the faradaic efficiency of O_2 was nearly 100%, confirming that the oxygen evolution reaction was the only reaction occurring at the Pt counter electrode in the anodic reactor.

The catalytic activity of the Bi/GaN/Si photocathodes was further investigated by tuning t_{Bi} (Fig. S17). At t_{Bi} = 2 nm, increments of FE_{HCOOH} and j_{HCOOH} were not noticeable compared to GaN/Si (t_{Bi} = 0 nm) (Fig. 4f). However, deposition of 5 nm-thick Bi NPs dramatically increased FE_{HCOOH} to 88.0%, 98.3%, and 94.7% at -0.2, -0.4, and -0.6 V_{RHE}, respectively. Accordingly, the maximum j_{HCOOH} = 10.3 mA/cm^2 was achieved at -0.6 V_{RHE}. At a higher loading of Bi NPs (t_{Bi} = 10 nm), FE_{HOOCH} and jHCOOH were slightly decreased to 87.0% and 8.2 mA/cm^2 at -0.6 V_{RHE}. The Bi NPs provide active sites for catalyzing the reaction. Thus, both FE_{HCOOH} and j_{HCOOH} first improved with t_{Bi}. However, overloading of Bi NPs can block the incident light and decrease the number of photogenerated electrons. The balance between the catalytic activity and optical transmittance of Bi NPs leads to an optimized thickness (t_{Bi} = 5 nm). The Bi/GaN/Si photocathode showed high FE_{HCOOH} > 90% for 12 h operation (Fig. S18). It is therefore seen that Bi/GaN/Si is a promising photocathode for PEC CO_2 RR with prolonged stability.

In order to gain more insights into the possible impact of interfacial interaction between GaN NWs and Bi NPs on the CO_2 RR activity, density functional theory (DFT) calculations were carried out. Based on the TEM and XPS results that the outermost surface of Bi NPs featured the oxidized Bi species in the form of Bi_2O_3, $Bi_2O_2CO_3$, or amorphous oxide/hydroxide, Bi_2O_3/GaN$(10\bar{1}0)$ model was established to elucidate the interfacial interaction. The geometries of GaN$(10\bar{1}0)$ and Bi_2O_3 were optimized by considering the PEC CO_2 RR in an aqueous condition (Fig. S19 and S20). Then, the free energy diagram of reducing CO_2 to HCOOH and CO with corresponding fully relaxed configuration was calculated. On the GaN$(10\bar{1}0)$ surface, the limiting potential (μ) for CO_2 reduction to HCOOH via *OCHO intermediate was 2.10 eV and the μ for CO production via *COOH intermediate was 1.93 eV (Fig. S21). Due to the large thermodynamic potential barriers, CO_2 RR on the GaN surface is unfavorable. On the other hand, self-supported Bi_2O_3 significantly stabilized *OCHO relative to *COOH, leading to dramatically reduced μ of 1.04 eV for HCOOH production (Fig. S22). Most strikingly, the μ value for HCOOH production was further lowered to 0.95 eV at the surface of Bi_2O_3/GaN$(10\bar{1}0)$ whereas high μ (1.93 eV) was retained for CO production (Fig. 5a), indicating that Bi_2O_3/GaN binary system predominantly converts CO_2 to HCOOH rather than CO. These results indicate that Bi_2O_3 cocatalyst supported on GaN NWs can greatly enhance the activity and selectivity of HCOOH. CO_2 RR by Bi/GaN/Si followed the same reaction pathway to that of previous Bi-based catalysts through *OCHO intermediate.[51, 52] However, it should be noted that Bi_2O_3/GaN binary systems can further lower the thermodynamic energy barrier for HCOOH production by stabilizing *OCHO intermediate compared to self-supported Bi_2O_3 or GaN. To visualize the strong electronic interaction between the Bi NPs and GaN NWs, the differential charge density at Bi_2O_3/GaN$(10\bar{1}0)$ interface was shown (Inset of Fig. 5a). After the junction, each interfacial Ga and Bi atoms lose Bader charge of 0.878e and 0.549e, respectively. Net charge transfer of 0.329e was observed at the Bi_2O_3/GaN interface. Electron reduction (blue) was found near the Ga atoms while electron accumulation (yellow) was found near the neighboring O atoms, revealing ionic Ga-O bond. Meanwhile, electrons accumulated at the middle region in between Bi and N atoms, suggesting the formation of covalent Bi-N bond. The Ga-O and Bi-N bonds resulted in the stable anchoring of Bi NPs on GaN NWs.

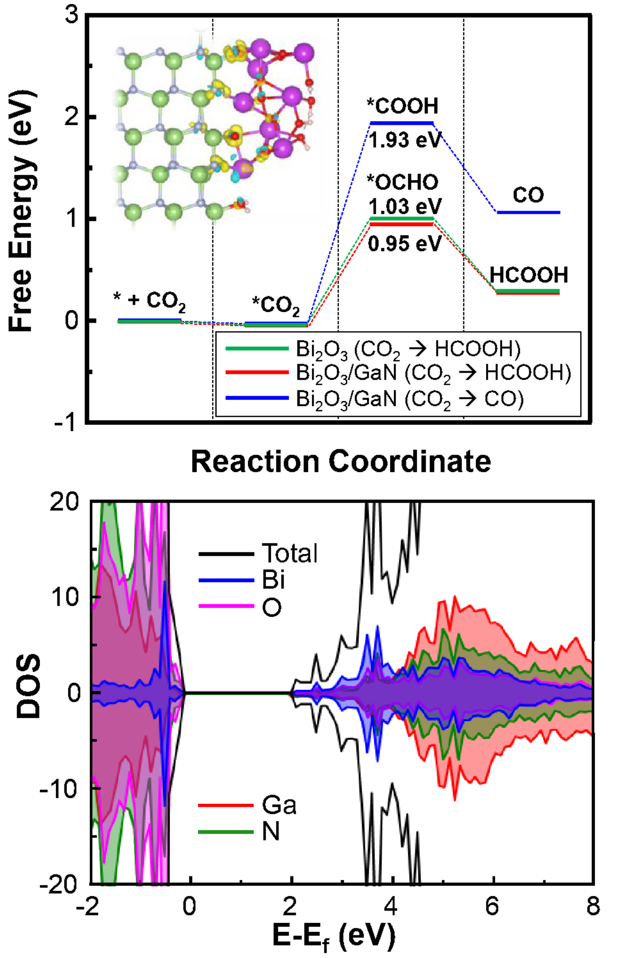

Fig. 5 (a) Free-energy profiles for CO_2 RR to HCOOH and CO on Bi_2O_3 and Bi_2O_3/GaN$(10\bar{1}0)$. Inset: differential charge density for Bi_2O_3/GaN$(10\bar{1}0)$ system. Blue: electron reduction, yellow: electron accumulation. (b) Density of states of Bi_2O_3/GaN$(10\bar{1}0)$.

Density of states (DOS) near the Fermi-level (E_f) of GaN was simulated for GaN and Bi_2O_3/GaN systems to investigate the electron transfer properties between GaN NWs and Bi NPs (Fig. S23). It is notable that the DOS at the conduction band edge ($2.3 < E-E_f < 4$ eV) was enlarged after the incorporation of Bi_2O_3 on the GaN. The enlarged DOS at this energy level was attributed to the atomic Bi and O (Fig. 5b), indicating that the energy states of Bi_2O_3 positions slightly lower than the conduction band edge of GaN. This conduction band alignment facilitates the spontaneous transfer of photoelectrons without notable charge carrier transfer resistance. The thermodynamically favorable HCOOH production on the Bi NPs and efficient charge carrier transfer from GaN NWs to Bi NPs induce photogenerated electrons to move towards the Bi NPs during the PEC CO_2 RR. Although the Bi_2O_3/GaN model cannot fully explain all possible combinations of Bi-GaN binary systems, it is still a very important finding that the synergetic effect of the semiconductor and the cocatalyst enhances the catalytic activity compared to each single material.

Previously, Bi-based electrocatalysts have demonstrated promising catalytic activity for CO_2 reduction to HCOOH by stabilizing the *OCHO intermediate. Interface engineering of two different materials has been an emerging strategy to promote catalytic performance. For instance, charge transfer at the interface between two different Bi-based materials led to optimizing the binding energy of adsorbates and lowered the thermodynamic energy barrier.[53, 54] The effect of semiconductor/cocatalyst interface on catalytic performance, however, has been rarely investigated even though there have been many reports of PEC CO_2 RR to HCOOH by integrating photocathodes and cocatalysts (Table S2). Thermodynamically feasible production of HCOOH by Bi_2O_3-GaN binary systems compared to each material of Bi_2O_3 and GaN revealed that the design rule of heterogeneous catalysis can be applied to PEC reactions. Compared to the previous photocathodes, Bi/GaN/Si photocathodes presented in this study exhibited excellent PEC CO_2 RR activity with a low onset-potential (0.2 V_{RHE}), high FE_{HCOOH} (98% at -0.3 V_{RHE}), j_{HCOOH} (10.3 mA/cm^2 at -0.6 V_{RHE}), and prolonged stability (12 h) due to beneficial Bi-GaN interaction. What is more, PEC CO_2 RR operated at a much lower applied bias than electrocatalysis using Bi-based electrocatalysts because the built-in-potential formed in photocathode (n^+-p Si) positively shifted the reduction potentials. In general, the design of photocathode is more difficult than the fabrication of an electrocatalyst because it is necessary to consider not only the catalytic activity but also the light absorption and the interfacial electronic interaction between semiconductor and cocatalyst. Nevertheless, Bi/GaN/Si photocathode showed excellent performance in terms of catalytic activity, optical transmittance, and electronic band alignment, establishing a highly promising architecture for efficient and stable solar-fuel production.

Conclusions

In summary, we have demonstrated that Bi NPs catalyst supported on GaN/Si photocathode is highly active and selective for PEC CO_2 RR toward HCOOH. This unique design allows efficient solar light absorption and charge carrier transport, and further exposes the abundant catalytic active sites. Theoretical calculations suggest that the binary system consisting of Bi NPs and GaN NWs works in synergy for CO_2 reduction and reduces the reaction energy barrier by stabilizing key reaction intermediates of OCHO*. As a result, Bi/GaN/Si photocathodes showed superior FE_{HCOOH} ~ 98.0% at -0.3 V_{RHE} and j_{HCOOH} = 10.3 mA/cm^2 at -0.6 V_{RHE}. Stable and continuous operation for 12 h was also demonstrated with a high FE_{HCOOH} > 90%. The electronic interactions between the semiconductor and the cocatalyst to enhance the catalytic activity will help rationally design photoelectrode in future. The photocathode consists of industry-ready materials (Si, GaN, Bi) provides a promising route for producing clean solar fuels from PEC CO_2 reduction in an aqueous cell.

Experimental

Fabrication of Bi/GaN/Si photoelectrode

n^+-p Si junction was firstly fabricated through a standard thermal diffusion process using (100) Si wafer. Phosphorus and boron dopants were coated on two opposite sides of the polished p-Si (100) wafer by spin-coating and then annealed at 950 ºC under nitrogen atmosphere for 4 h. Plasma-assisted MBE was used for growing GaN NWs on Si wafer under nitrogen rich-condition with a N_2 flow rate of 1.0 standard cubic centimeter per minute. The substrate temperature was 790 ºC and the growth duration was ~2 h. The forward plasma power was 350 W with Ga flux beam equivalent pressure (BEP) of 5×10^{-8} Torr. Bi NPs were deposited on GaN NWs/Si by a thermal evaporation method with a deposition rate of 0.1 nm/s under a base pressure of 1×10^{-6} Torr. The rate and thickness of the Bi were in situ monitored by a quartz crystal thickness monitor. Also, the thickness of Bi film was double-checked on planar Si wafer by surface profiler.

Structural and optical characterization

SEM and EDS analysis were conducted using a PHILIPS XL30S with an accelerating voltage of 5 kV and a working distance of 6 mm. HR-TEM and STEM equipped with an energy-loss spectrometer were conducted at 200 kV with Cs-corrector using JEOL JEM 2200FS. XPS was measured using a Thermo ESCALAB250i X-ray photoelectron spectrometer with a monochromatic Al Kα source at a base pressure < 2×10^{-9} Torr. Optical reflectance and transmittance were measured using a UV-visible spectrometer (Agilent Technologies Cary 4000) equipped with integrating sphere. Optical reflectance of polytetrafluoroethylene (PTFE) standard reflector was calibrated to 100% and that of sample was calculated with the following equation:

$$\mathrm{OR} = \frac{I_{sample}}{I_{PTFE}} \times 100\%$$

where I_{sample} and I_{PTFE} are the detected light intensity reflected by the sample and PTFE standard reflector, respectively.

Photoelectrochemical measurements

LSV measurements were conducted in an H-type cell separated by a nafion membrane with a three-electrode system using a potentiostat (Ivium Stat). Ag/AgCl filled with 3 M KCl was used as the reference electrode and Pt mesh was used as the counter electrode. Photocathodes were used as the working electrodes. The electrolyte used for PEC measurements was an aqueous solution of 0.1 M $KHCO_3$ (Sigma-Aldrich, 99.95%) prepared by dissolving the solid salt in deionized water. The electrolyte was saturated with CO_2 gas (99.99%) before the measurements. The measured potential ($V_{Ag/AgCl}$) (V) can be converted to the reversible hydrogen electrode (V_{RHE}) (V) by using the Nernst function: $V_{RHE} = V_{Ag/AgCl} + 0.222 + 0.0592 \times \mathrm{pH}$. The light source used for the illumination was LS 150 Xenon Arc Lamp (ABET Technologies). The light intensity (100 mW/cm^2) was calibrated using a mono-silicon detector by the National Renewable Energy Laboratory. All measurements were conducted under ambient pressure at room temperature.

Product analysis

Gas products were analyzed using a gas chromatographer (Inficon, 3000 Micro GC) equipped with two thermal conductivity detectors (TCD) connected to Molsieve column and Plot U column. Before beginning the PEC CO_2 RR, the apparatus was purged with CO_2 gas for 3 min to remove other gases. During the reaction, gas was circulated within the reactor at a flow rate of 50 ml/min. After the reaction, gas products were automatically pumped into the gas chromatographer for analysis. Liquid products (HCOOH) were analyzed using a 500 MHZ 1H 1D liquid NMR spectrometer (Bruker) at 25 °C. The standard solution was 5 mM N,N-dimethylformamide (Sigma-Aldrich) in D_2O (Sigma-Aldrich). The amount of HCOOH was calculated by integrating areas of the products with that of standard solution.

Calculations

First-principles density functional theory (DFT) calculations were performed with the projector augmented wave (PAW) method and the generalized gradient approximation of Perdew, Burke, and Ernzerhof (PBE) for exchange-correlation potential and implemented in Vienna Ab initio Simulation Package (VASP) code.[55, 56] The conventional DFT energy was corrected by Grimme's method (D3) in order to describe van der Waals interaction properly.[57] Dipole correction along the slab cell c-axis was employed due to the asymmetric layer arrangement. All GaN, Bi_2O_3 and Bi_2O_3/GaN composite slabs were constructed from the fully relaxed bulk structure of GaN and Bi_2O_3. Based on the crystallographic direction of GaN NW and surface energy of Bi_2O_3,[58] surface vacuum slab with $(10\bar{1}0)$ and (010) surface were fabricated, respectively. The thickness of the GaN and Bi_2O_3 slabs were controlled to be at least 12 Å, composed of 5 unit cells periodically along the direction perpendicular to surface. To mimic the bulk-like property, the bottom 2 layers were fixed while the surface 3 layers were fully relaxed. For GaN-Bi_2O_3 composite slab, to alleviate the computational load, the thickness of the GaN slab was reduced to 3 layers. A (010) surface of Bi_2O_3 single unit cell was placed on the most energetically favorable site of fully relaxed GaN$(10\bar{1}0)$surface followed by complete relaxation. Vacuum region of slab cells was set to be more than 15 Å, to avoid the artificial interaction between periodic images. For the GaN and Bi_2O_3/GaN slab with rectangular cell modeling, monkhorst-Pack k-point sampling with a grid of 4 × 2 × 1 was used for the Brillouin zone integration.[59] In the case of monoclinic Bi_2O_3, gamma-centered k-point sampling of 4 × 4 × 1 was employed. An energy cutoff of 400 eV was used for the plane-wave representation of the wavefunctions. Atomic structures were relaxed until all the Hellman-Feynman forces were < 0.01 eV/Å and the criterion for the electronic step convergence was 10^{-5}.

Author Contributions

W.J. Dong conceived the idea and designed the experiments. W.J Dong and I.A. Navid fabricated the photocathodes. Y. Xiao contributed for characterization of GaN NWs. T.H. Lee conducted DFT calculation. J.W. Lim participated in evaluation of CO_2 reduction performance. D. Lee provided guidance on DFT calculation. H.W. Jang supervised theoretical calculation. J.-L. and Z. Mi supervised the work. All authors participated to the discussion of the results.

Conflicts of interest

Some IP related to this work was licensed to NS Nanotech, Inc. and NX Fuels, Inc., which were co-founded by Z. Mi. The University of Michigan and Mi have a financial interest in the companies.

Acknowledgements

This work was supported by the Basic Science Research Program through the NRF of Korea funded by the Ministry of Education (2020R1I1A1A01069108), in part by the Korea Institute of Energy Technology Evaluation and Planning (KETEP) and the Ministry of Trade, Industry & Energy (MOTIE) of the Republic of Korea (20212010100040), in part by the National Research Foundation of Korea (NRF) grant funded by the Korea government (MSIT) (No. 2019R1A2C1091158). The work conducted at the University of Michigan was supported by the Blue Sky program in the College of Engineering and by US Army Research Office Award W911NF2110337.

References

1. M. B. Ross, P. De Luna, Y. Li, C.-T. Dinh, D. Kim, P. Yang and E. H. Sargent, *Nat. Catal.*, 2019, **2**, 648-658.
2. M. Schreier, F. Héroguel, L. Steier, S. Ahmad, J. S. Luterbacher, M. T. Mayer, J. Luo and M. Grätzel, *Nat. Energy*, 2017, **2**, 1-9.
3. W. J. Dong, J. W. Lim, D. M. Hong, J. Kim, J. Y. Park, W. S. Cho, S. Baek and J.-L. Lee, *ACS Appl. Mater. Interfaces*, 2021, **13**, 18905-18913.
4. L. Fan, C. Xia, P. Zhu, Y. Lu and H. Wang, *Nat. Commun.*, 2020, **11**, 1-9.
5. R. Kamata, H. Kumagai, Y. Yamazaki, M. Higashi, R. Abe and O. Ishitani, *J. Mater. Chem. A*, 2021, **9**, 1517-1529.
6. Y. Y. Birdja, E. Pérez-Gallent, M. C. Figueiredo, A. J. Göttle, F. Calle-Vallejo and M. T. Koper, *Nat. Energy*, 2019, **4**, 732-745.
7. T.-T. Zhuang, Z.-Q. Liang, A. Seifitokaldani, Y. Li, P. De Luna, T. Burdyny, F. Che, F. Meng, Y. Min and R. Quintero-Bermudez, *Nat. Catal.*, 2018, **1**, 421-428.
8. Y. Zheng, A. Vasileff, X. Zhou, Y. Jiao, M. Jaroniec and S.-Z. Qiao, *J. Am. Chem. Soc.*, 2019, **141**, 7646-7659.
9. K. D. Yang, Y. Ha, U. Sim, J. An, C. W. Lee, K. Jin, Y. Kim, J. Park, J. S. Hong and J. H. Lee, *Adv Funct. Mater.*, 2016, **26**, 233-242.
10. K. R. Rao, S. Pishgar, J. Strain, B. Kumar, V. Atla, S. Kumari and J. M. Spurgeon, *J. Mater. Chem. A*, 2018, **6**, 1736-1742.
11. J. J. Leung, J. Warnan, K. H. Ly, N. Heidary, D. H. Nam, M. F. Kuehnel and E. Reisner, *Nat. Catal.*, 2019, **2**, 354-365.
12. T. Arai, S. Sato, T. Kajino and T. Morikawa, *Energy Environ. Sci.*, 2013, **6**, 1274-1282.
13. J. S. DuChene, G. Tagliabue, A. J. Welch, X. Li, W.-H. Cheng and H. A. Atwater, *Nano Lett.*, 2020, **20**, 2348-2358.
14. J. Hou, H. Cheng, O. Takeda and H. Zhu, *Angew. Chem. Int. Ed.*, 2015, **54**, 8480-8484.
15. M. Schreier, P. Gao, M. T. Mayer, J. Luo, T. Moehl, M. K. Nazeeruddin, S. D. Tilley and M. Grätzel, *Energy Environ. Sci.*, 2015, **8**, 855-861.
16. L. Vayssieres, *On solar hydrogen and nanotechnology*, John Wiley & Sons, 2010.
17. M. J. Choi, J.-Y. Jung, M.-J. Park, J.-W. Song, J.-H. Lee and J. H. Bang, *J. Mater. Chem. A*, 2014, **2**, 2928-2933.
18. J. T. Song, H. Ryoo, M. Cho, J. Kim, J. G. Kim, S. Y. Chung and J. Oh, *Adv. Energy Mater.*, 2017, **7**, 1601103.
19. C. Li, T. Wang, B. Liu, M. Chen, A. Li, G. Zhang, M. Du, H. Wang, S. F. Liu and J. Gong, *Energy Environ. Sci.*, 2019, **12**, 923-928.
20. M. Kan, Z. W. Yan, X. Wang, J. L. Hitt, L. Xiao, J. M. McNeill, Y. Wang, Y. Zhao and T. E. Mallouk, *Angew. Chem. Int. Ed.*, 2020, **59**, 11462-11469.
21. L. Wei, J. Lin, S. Xie, W. Ma, Q. Zhang, Z. Shen and Y. Wang, *Nanoscale*, 2019, **11**, 12530-12536.
22. Q. Kong, D. Kim, C. Liu, Y. Yu, Y. Su, Y. Li and P. Yang, *Nano Lett.*, 2016, **16**, 5675-5680.
23. J. W. Beeman, J. Bullock, H. Wang, J. Eichhorn, C. Towle, A. Javey, F. M. Toma, N. Mathews and J. W. Ager, *Energy Environ. Sci.*, 2019, **12**, 1068-1077.
24. S. K. Choi, U. Kang, S. Lee, D. J. Ham, S. M. Ji and H. Park, *Adv. Energy Mater.*, 2014, **4**, 1301614.
25. P. Ding, Y. Hu, J. Deng, J. Chen, C. Zha, H. Yang, N. Han, Q. Gong, L. Li and T. Wang, *Mater. Today Chem.*, 2019, **11**, 80-85.
26. S. Liu, X. F. Lu, J. Xiao, X. Wang and X. W. Lou, *Angew. Chem. Int. Ed.*, 2019, **58**, 13828-13833.
27. S. Vanka, E. Arca, S. Cheng, K. Sun, G. A. Botton, G. Teeter and Z. Mi, *Nano Lett.*, 2018, **18**, 6530-6537.
28. S. Chu, S. Fan, Y. Wang, D. Rossouw, Y. Wang, G. A. Botton and Z. Mi, *Angew. Chem. Int. Ed.*, 2016, **55**, 14262-14266.
29. B. Zhou, X. Kong, S. Vanka, S. Cheng, N. Pant, S. Chu, P. Ghamari, Y. Wang, G. Botton and H. Cuo, *Energy Environ. Sci.*, 2019, **12**, 2842-2848.
30. B. Zhou, P. Ou, N. Pant, S. Cheng, S. Vanka, S. Chu, R. T. Rashid, G. Botton, J. Song and Z. Mi, *Proc. Natl. Acad. Sci. U. S. A.*, 2020, **117**, 1330-1338.
31. W. J. Dong, I. A. Navid, Y. Xiao, J. W. Lim, J.-L. Lee and Z. Mi, *J. Am. Chem. Soc.*, 2021, **143**, 10099-10107.
32. S. Kattel, P. J. Ramírez, J. G. Chen, J. A. Rodriguez and P. Liu, *Science*, 2017, **355**, 1296-1299.
33. J. C. Matsubu, S. Zhang, L. DeRita, N. S. Marinkovic, J. G. Chen, G. W. Graham, X. Pan and P. Christopher, *Nat. Chem.*, 2017, **9**, 120-127.
34. D. Gao, Y. Zhang, Z. Zhou, F. Cai, X. Zhao, W. Huang, Y. Li, J. Zhu, P. Liu and F. Yang, *J. Am. Chem. Soc.*, 2017, **139**, 5652-5655.
35. Y. Y. Birdja, R. l. E. Vos, T. A. Wezendonk, L. Jiang, F. Kapteijn and M. T. Koper, *ACS Catal.*, 2018, **8**, 4420-4428.
36. J.-H. Kim, H. Woo, J. Choi, H.-W. Jung and Y.-T. Kim, *ACS Catal.*, 2017, **7**, 2101-2106.
37. S. Li, Y. Xu, Y. Chen, W. Li, L. Lin, M. Li, Y. Deng, X. Wang, B. Ge, C. Yang, S. Yao, J. Xie, Y. Li, X. Liu and D. Ma, *Angew. Chem. Int. Ed.*, 2017, **56**, 10761-10765.
38. W. J. Dong, C. J. Yoo, J. W. Lim, J. Y. Park, K. Kim, S. Kim, D. Lee and J.-L. Lee, *Nano Energy*, 2020, **78**, 105168.
39. P. Zhang, X. F. Lu, D. Luan and X. W. Lou, *Angew. Chem. Int.*

Ed., 2020, **59**, 8128-8132.

40. D. Kopač, B. Likozar and M. Huš, *ACS Catal.*, 2020, **10**, 4092-4102.
41. Y. Wang, P. Han, X. Lv, L. Zhang and G. Zheng, *Joule*, 2018, **2**, 2551-2582.
42. S. Zhang, P. Kang and T. J. Meyer, *J. Am. Chem. Soc.*, 2014, **136**, 1734-1737.
43. T. Lei, M. Fanciulli, R. Molnar, T. Moustakas, R. Graham and J. Scanlon, *Appl. Phys. Lett.*, 1991, **59**, 944-946.
44. C. W. Lee, J. S. Hong, K. D. Yang, K. Jin, J. H. Lee, H.-Y. Ahn, H. Seo, N.-E. Sung and K. T. Nam, *ACS Catal.*, 2018, **8**, 931-937.
45. P. Deng, H. Wang, R. Qi, J. Zhu, S. Chen, F. Yang, L. Zhou, K. Qi, H. Liu and B. Y. Xia, *ACS Catal.*, 2019, **10**, 743-750.
46. S. Wolter, B. Luther, D. Waltemyer, C. Önneby, S. E. Mohney and R. Molnar, *Appl. Phys. Lett.*, 1997, **70**, 2156-2158.
47. T. Duan, J. Pan and D. S. Ang, *Appl. Phys. Lett.*, 2013, **102**, 201604.
48. S. Kim, W. J. Dong, S. Gim, W. Sohn, J. Y. Park, C. J. Yoo, H. W. Jang and J.-L. Lee, *Nano Energy*, 2017, **39**, 44-52.
49. S. L. Diedenhofen, G. Vecchi, R. E. Algra, A. Hartsuiker, O. L. Muskens, G. Immink, E. P. Bakkers, W. L. Vos and J. G. Rivas, *Adv. Mater.*, 2009, **21**, 973-978.
50. N. Han, Y. Wang, H. Yang, J. Deng, J. Wu, Y. Li and Y. Li, *Nat. Commun.*, 2018, **9**, 1-8.
51. J. H. Koh, D. H. Won, T. Eom, N.-K. Kim, K. D. Jung, H. Kim, Y. J. Hwang and B. K. Min, *ACS Catal.*, 2017, **7**, 5071-5077.
52. W. Zhang, Y. Hu, L. Ma, G. Zhu, P. Zhao, X. Xue, R. Chen, S. Yang, J. Ma and J. Liu, *Nano Energy*, 2018, **53**, 808-816.
53. G. Wen, D. U. Lee, B. Ren, F. M. Hassan, G. Jiang, Z. P. Cano, J. Gostick, E. Croiset, Z. Bai and L. Yang, *Adv. Energy Mater.*, 2018, **8**, 1802427.
54. P. F. Sui, C. Xu, M. N. Zhu, S. Liu, Q. Liu and J. L. Luo, *Small*, 2021, 2105682.
55. J. P. Perdew, K. Burke and M. Ernzerhof, *Phys. Rev. Lett.*, 1996, **77**, 3865.
56. P. E. Blöchl, *Phys. Rev. B*, 1994, **50**, 17953.
57. S. Grimme, S. Ehrlich and L. Goerigk, *J. Comput. Chem.*, 2011, **32**, 1456-1465.
58. Y.-H. Lei and Z.-X. Chen, *J. Chem. Phys.*, 2013, **138**, 054703.
59. H. J. Monkhorst and J. D. Pack, *Phys. Rev. B*, 1976, **13**, 5188.

This journal is © The Royal Society of Chemistry 20xx